Direct observation of important morphology and composition changes at the surface of the CuO conversion material in lithium batteries

Lucile Martin [a,b], Hervé Martinez [a,*], Delphine Poinot [b,c], Brigitte Pecquenard [c], Frédéric Le Cras [b]

[a] IPREM ECP – UMR5254, Université de Pau et des Pays de l'Adour, Hélioparc Pau-Pyrénées, 2 Av du Président Pierre Angot, 64053 Pau Cedex 9, France
[b] CEA LITEN, 17 Rue des Martyrs, 38054 Grenoble, France
[c] CNRS ICMCB site de l'ENSCBP, Université de Bordeaux, 87 Av du Dr. Schweitzer, 33608 Pessac Cedex, France

HIGHLIGHTS

- Study of surface changes occurring during the cycling of a CuO thin film electrode.
- A SEI characterized by a LiF-rich inner layer and a Li_2CO_3-rich outer layer.
- Formation/partial dissolution of carbonates species was evidenced.
- Formation/disappearance of large "spherical" particles was observed at the surface.
- Mechanisms are proposed to explain the important morphological changes.

ARTICLE INFO

ABSTRACT

Morphology and composition changes occurring at the surface of CuO thin film electrode, used as conversion material for lithium-ion battery, were investigated at different stages of the electrochemical cycling by atomic force microscopy (AFM) and X-ray photoelectron spectroscopy (XPS). Analyses were performed on samples obtained in $LiPF_6$ containing carbonate-based electrolyte and prepared by linear sweep voltammetry. The formation/partial dissolution of a solid electrolyte interphase (SEI) was evidenced by XPS analyses. The SEI layer formed on lithiated CuO thin film during the first reduction between [3.5–0.8] $V/Li^+/Li$ is characterized by a LiF-rich inner layer and a Li_2CO_3-rich outer layer. Furthermore, reduction/oxidation cycles induced important surface morphology modifications. In particular, the growth and then the vanishing of large spherical nodules (~400 nm in diameter) were observed during the lithium insertion and the subsequent deinsertion. During the twenty first cycles performed, even if a stable electrochemical behavior was shown, breathing of the thin film was also clearly evidenced by AFM images with the appearance and disappearance of numerous cracks as a function of Li removal and Li insertion processes.

1. Introduction

The increasing need for highly efficient power sources suitable for numerous devices, from microelectronics to transportation, has induced intense research efforts in order to improve the performances of Li-ion batteries. The specific capacity of intercalation compounds, commonly used as electrode materials, is limited by the number of available sites for lithium ions in the crystal structure, generally not exceeding 1 Li/transition metal. Other electrode materials (i.e. transition metal compounds MX_y (M = Co, Fe, Ni, Cu, etc.; X = F, O, S, etc.)), in which the insertion of lithium proceeds through a so-called conversion mechanism [1], can electrochemically react with a far larger Li amount and have received an increasing attention these last ten years. Lithium insertion leads to the transformation of the initial transition metal compound MX_y into M^0 nanoparticles surrounded by a yLi_nX matrix and the number of Li ions exchanged per transition metal can be formally as high as y*n (n being the formal charge of the ligand) according to the following mechanism [2]:

$$MX_y + (y*n)Li \Leftrightarrow yLi_nX + M$$
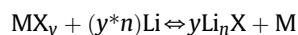
* Corresponding author. Tel.: +33 5 59 40 75 99; fax: +33 5 59 40 76 22.
  E-mail address: herve.martinez@univ-pau.fr (H. Martinez).

This mechanism was recently found to be reversible for some of these materials [1] and renewed the interest for their use as negative electrode materials in high energy density Li-ion cells.

Among the transition metal oxides (MO_y) studied as conversion material electrodes, CuO is well known because of its use as a positive electrode in primary commercial CuO/Li cells having a discharge voltage between 1.4 and 1.0 V [3]. Since Tarascon et al. [4,5] have first reported the reversible conversion reactivity of CuO particles with lithium, copper(II) oxide appears as an attractive electrode material because of its low cost, non-toxicity, high theoretical specific capacities (674 mAh g^{-1} and 4260 mAh cm^{-3}) and its ability to be easily prepared in a thin film form. Morales et al. [6] have previously studied nanostructured CuO thin films prepared by spray pyrolysis and tested them as electrode in lithium cells. They have evaluated the electrochemical behavior in function of the thin film physical properties and evidenced that the film with the smallest grain size was able to supply sustained specific capacity as high as 625 mAh g^{-1}. Moreover, the redox mechanisms which occur into CuO thin films during the lithiation/delithiation process were identified in a previous paper [7].

In liquid electrolyte cell, solvents and salt usually undergo competing and parallel reduction processes below a given potential (around 1.3 V/Li$^+$/Li in conventional electrolytes) which result in the deposition of various organic and inorganic products on the electrode surface during the electrochemical cycling. The physical and chemical properties of this complex layer strongly influence both the reversible capacity and the cycle life of the cell by its ability to passivate the electrode. In the case of graphite electrode, models of the Solid Electrolyte Interphase (SEI) were proposed by Peled et al. [8], Aurbach et al. [9,10], and Edström et al. [11] when classical carbonate-based electrolytes with LiPF$_6$ salt are used. They have suggested that SEI is a dense layer made of inorganic components close to the electrode surface (consisting mainly of Li_2O, LiF and Li_2CO_3), and of a porous organic or polymeric layer close to interface with electrolyte. Numerous studies were reported in the literature dealing with the SEI formed on carbon anode materials [12–14]. Our group also reported several thorough XPS analyses of the SEI formed on different cathode and anode materials. However, few articles reported detailed studies about SEI formation and its evolution upon cycling for conversion material electrodes (Cr_2O_3 [15–17] and CoO [18]) and mechanisms are not fully understood. Indeed, the surface reactivity of these lithiated conversion materials is very specific as the generated metal nanoparticles can catalytically enhance electrolyte degradation [19].

The main objective of this work is then to improve the understanding of interfacial phenomena at conversion material electrode surface which present specific reactivity [19]. CuO thin films were prepared by sputtering and were used as a model electrode to get direct information on the CuO surface evolution (chemical nature and morphology) upon cycling, as parasitic effects or limitations due to binders or conducting additive materials are excluded. The surface composition and morphology of these CuO thin films were characterized at different discharge/charge potentials by means of X-ray photoelectron spectroscopy (XPS) and atomic force microscopy (AFM) with the same approach as our previous works on V_2O_5 [20] and Si [21] thin film electrodes. Then, correlations were established between the different evolutions observed for the SEI layer composition and the surface morphology during the electrochemical cycling.

2. Experimental

2.1. CuO thin film preparation

CuO thin films were prepared by reactive radio frequency magnetron sputtering using a copper target in (Ar + O_2)

atmosphere (Plassys MP700 device). All the stainless steel substrates were first cleaned by isopropanol vapor before their introduction in the deposition chamber. Before deposition, the substrates were also etched by argon ions using an ion beam and then the target was pre-sputtered during 15 min in the Ar–O_2 atmosphere. During the deposition, the power density applied to the target was fixed to 2.3 W cm^{-2}, the total flow rate was kept at 50 sccm and the oxygen flow rate at 6 sccm. A total pressure of 1 Pa was applied and the substrate holder was rotating to get homogeneous thin films. The substrates were not heated intentionally. Note that the XRD pattern obtained for the elaborated thin films allows an accurate identification of the main CuO phase and only exhibits some Cu_2O impurities (see Supporting information).

2.2. Electrochemical measurements

Electrochemical characterizations were performed in CR2032–type coin cells containing the CuO working electrode. The thickness of the CuO thin films used for the cycling was measured with a profilometer and is around 500 nm. The mass of each CuO thin film (ca. 400 μg) was precisely measured with a microbalance before coin cell assembly (accuracy equal to ±2 μg). A lithium foil (Chemetall) was used as the negative electrode. The electrolyte was 1 M LiPF$_6$ in a 1:1:3 volumetric mixture of ethylene carbonate (EC), propylene carbonate (PC) and dimethyl carbonate (DMC), with 2 wt % of vinylene carbonate (VC) (Novolyte). A polypropylene microporous membrane (Celgard 2400) associated with a non-woven polypropylene felt (Viledon, Freudenberg) was used as separator. The electrochemical experiments were carried out with a VMP galvanostat/potentiostat (Bio-Logic) at 25 °C. Cyclic voltammetry was used to perform the two first cycles between 0.8 and 3.5 V *vs* Li$^+$/Li at a scan rate of 5 μV s^{-1} and then further cycles were achieved at a constant current density of 6.6 μA cm^{-2} (up to 20 cycles). All Li$_x$CuO electrodes were extracted from the cell and then washed with fresh DMC to remove residual electrolyte solvents and salt. The Li content (x) was determined from specific capacities with a typical deviation of 10%. Cell assembly, disassembly and electrode washing processes were carried out in an argon filled glove box. Samples were packaged in airtight glass tubes under argon and introduced in the glove box of the corresponding characterization apparatus (XPS, AFM) or transferred through an airtight system into the scanning electron microscope chamber.

2.3. XPS analysis

X-ray photoelectron spectroscopy (XPS) measurements were carried out with a Thermo K-alpha spectrometer using a microfocused monochromatized Al Kα radiation ($h\nu$ = 1486.7 eV). The XPS spectrometer was directly connected to an argon dry box in order to avoid any moisture and air exposure of the samples. The residual pressure inside the analysis chamber was 1.10^{-9} mbar. The spectrometer was calibrated using the photoemission lines of Ag 3d$_{5/2}$, Au 4f$_{7/2}$ and Cu 2p$_{3/2}$. The peaks were recorded with constant pass energy of 30 eV. The diameter of the irradiated area of the sample was 200 μm. Charging effects were minimized by the use of a dual beam charge neutralization system which combines low energy electrons and Ar$^+$ ions to provide efficient charge compensation. In order to check that sample was not damaged by X-rays, one scan per element was collected before and after XPS core peaks acquisition performed on a sample. All spectra were energy calibrated by using the hydrocarbon peak at a binding energy of 285.0 eV. The Casa software was used to fit photoelectron spectra using a least squares algorithm. The background in narrow range spectra was accommodated by a nonlinear Shirley function [22]. The experimental curves were fitted using combinations of

Gaussian (70%) and Lorentzian (30%) distributions. Quantification was performed on the basis of Scofield's relative sensitivity factors [23].

2.4. Morphology characterizations

Atomic force microscopy (AFM) imaging was performed with a MultiMode Scanning Probe Microscope (MM-SPM) from Veeco society and a controller Nanoscope IIIA and Quadrex. This Microscope was placed in a glove box (argon atmosphere) in order to avoid surface contamination of the samples during analyses (oxygen and water levels lower than 1 ppm). All AFM images were acquired in intermittent contact mode (tapping) to obtain topographic (with a scanning frequency from 0.4 to 1.0 Hz), phase and amplitude (error signal) images. Two different Veeco probes which have a quoted tip radius of curvature lower than 10 nm were used to obtain the best image resolution in function of the surface morphology. First, when faceting nanograins are present at the surface, a silicon probe with a force of 40 N m^{-1} at a resonance frequency of about 300 kHz was employed (MPP11100). Secondly, when spherical nanograins or larger grains are observed at the surface, a silicon probe with a force of 5 N m^{-1} at a resonance frequency of about 150 kHz was chosen (MPP12100). Note that the characteristics of these probes were chosen to maximize the signal/noise ratio in each case. Quantitatively, the surface roughness can be determined with the use of the so-called RMS (root mean square) roughness R_q which is the standard deviation of the Z (height) values within a given area. The R_q parameter is calculated from several zones of the sample and is evaluated by taking into account 6 measurements with a typical deviation of 5%. To complete the quantitative analysis, the size of the grains and the dimensions of the cracks were evaluated by taking into account 40 measurements performed on different topographic linear profiles.

SEM images of the surface and cross-section were obtained with a JEOL 6700-F FEG-SEM on CuO thin films deposited on stainless steel substrate, previously covered by a gold thin film to avoid any charging effect.

3. Results and discussion

3.1. Chemical and morphological evolution during the first cycle

Fig. 1 depicts the first reduction/oxidation cycle of a CuO thin film/Li cell. The electrochemical processes were studied through the acquisition of various XPS spectra and AFM images recorded at different stages of the first cycle (see dots on the Fig. 1 where red dots (in web version) correspond to reduction and blue ones to oxidation). In a previous paper [7], we studied the redox processes by XPS analyses after erosion for the samples numbered 1 to 6. As the analysis depth of the XPS technique is about 5 nm, mechanical erosion was thus used to remove the organic/inorganic passivating layer present at the surface of cycled electrodes and to efficiently probe the active electrode material. A new mechanism was then proposed for the conversion reaction of CuO with Li, successively leading to Cu$^+$ and Cu^0 species and involving a 'Li$_2$O$_2$' peroxide type phase as an intermediate, whereas Li$_2$O is the main lithiated oxide at the end of the discharge. Three reduction steps (numbered I to III on Fig. 1) can be expressed by the following equations:
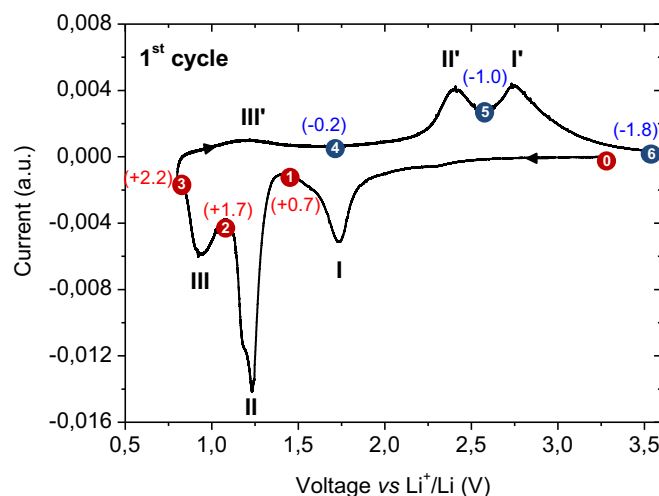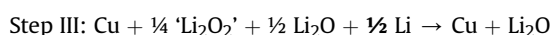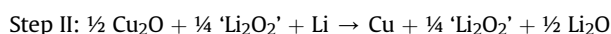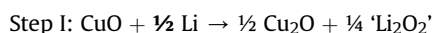
Step I: CuO + ½ Li → ½ Cu$_2$O + ¼ 'Li$_2$O$_2$'

Step II: ½ Cu$_2$O + ¼ 'Li$_2$O$_2$' + Li → Cu + ¼ 'Li$_2$O$_2$' + ½ Li$_2$O

Step III: Cu + ¼ 'Li$_2$O$_2$' + ½ Li$_2$O + ½ Li → Cu + Li$_2$O

Fig. 1. Voltammogram of the first cycle of a Li/CuO cell performed between 0.8 V and 3.5 V at a scan rate of 5.0 μV s^{-1}. The dots indicate the samples studied by XPS at different stages of the first cycle, with the corresponding number of Li ions (values between brackets) that have reacted with the electrode or that have been removed from the electrode.

During the first charge, the full reoxidation of Cu$_2$O into CuO was not observed in our experimental conditions.

3.1.1. XPS

Besides this previous study, thorough XPS analyses were systematically carried out without any erosion to probe the CuO thin film electrode/electrolyte interface. A first important result is related to the disappearance of the copper signal on XPS spectra obtained on all samples (from 1 to 6). This indicates that an organic/inorganic layer with a thickness higher than the XPS analysis depth (~5 nm) is formed from the beginning of the first discharge (above 1.4 V/Li$^+$/Li) and remains present on the electrode surface even after a reoxidation at 3.5 V/Li$^+$/Li.

XPS core peaks (C1s, O1s, Li1s, F1s, P2p) were recorded at different discharge/charge potentials (points indicated in Fig. 1). For a non exhaustive presentation, Table 1 and Fig. 2 only display results obtained for some selected points (0, 1, 3 and 6). Indeed, similar qualitative and quantitative results were obtained for points 2, 3, 4 and 5, showing that the composition of the outer SEI layer does not significantly change from the discharge potential of 1.0 V/Li$^+$/Li (point 2) to the charge potential of 2.6 V/Li$^+$/Li (point 5). We have thus chosen to detail the XPS results obtained at the end of the first discharge (point 3).

The C 1s core peak (Fig. 2a) provides valuable information regarding the SEI nature and is jointly analyzed with the O 1s (Fig. 2b) and Li 1s core peaks. Moreover, the F 1s and P 2p core peaks collected at point 1 and point 6 are presented in Fig. 3.

For the pristine sample, the C 1s signal exhibits a main component at 285.0 eV (C1: C−C, C−H) attributed to contaminating hydrocarbon always detected on the extreme surface, and to carbon atoms of organic species bound to carbon or hydrogen only. The asymmetry observed at 286.3 eV can be assigned to carbon atoms bound to one oxygen atom (C2: C−O), while the small component at 288.4 eV corresponds to carbon atoms characterized by a C=O bond (C3). These peaks are due to adsorbed species at the surface of the as-deposited CuO thin film. Concerning the O 1s core peak, the main component at 529.6 eV corresponds to oxygen atoms in the CuO lattice (O material) in agreement with previous papers [24,6]. Furthermore, the noticeable shoulder on the higher binding energy side, located at 531.5 eV, mainly arises from −OH surface species

Table 1
Quantitative XPS analyses performed onto CuO thin film electrodes at different stages of the first voltammetric cycle: before cycling (CuO reference sample), after a discharge down to 1.4 V/Li$^+$/Li (point 1), at the end of the discharge (point 3) and at the end of the charge (point 6).

Potential (V/Li$^+$/Li)		B.E. (eV) (FWHM)	at. %		B.E. (eV) (FWHM)	at. %
Before cycling **CuO thin film**	**C1s**			**O1s**		
	C1 (C–C, C–H)	285.0 (1.2)	24.7	**O material**	529.6 (1.0)	26.0
	C2 (C–O)	286.3 (1.4)	3.3	**–OH**	531.5 (1.6)	12.3
	C3 (C=O)	288.4 (1.4)	2.5	**C–O**	533.2 (1.6)	1.6
			30.5			**39.9**
				Cu 2p$_{3/2}$	933.6 (2.4) + satellites	29.6
Point 1, 1.4 V	**C1s**			**O1s**		
	C1 (C–C, C–H)	285.0 (1.5)	12.3	**O1 (P=O)**	531.2 (1.5)	2.2
	C2 (C–O)	286.9 (1.7)	1.4	**O2 (P–O$^-$)**	532.1 (1.5)	4.1
	C3 (O=C–O)	289.3 (1.7)	0.6	**O3 (C–O)**	533.6 (1.6)	1.3
			14.3			**8.5**
				Li1s	56.3 (1.4)	43.3
				F1s	685.6 (1.5)	30.5
					687.7 (1.7)	1.6
				P 2p$_{3/2}$	134.2 (2.2)	1.6
					137.1 (2.2)	0.2
Point 3, 0.8 V	**C1s**			**O1s**		
	C1 (C–C, C–H)	285.0 (1.4)	27.3	**O1 (CO$_3$)**	532.0 (1.5)	27.0
	C2 (C–O)	286.7 (1.4)	1.9	**O2 (C-O)**	533.7 (1.5)	1.5
	C3 (O=C–O)	289.1 (1.4)	1.7			**31.8**
			8.3			
	C4 (CO$_3$)	290.3 (1.2)	**39.2**	**Li1s**	55.6 (1.6)	29.0
				F1s	–	–
				P2p$_{3/2}$	–	–
Point 6, 3.5 V	**C1s**			**O1s**		
	C1 (C–C, C–H)	285.0 (1.3)	6.8	**O1 (CO$_3$)**	532.0 (1.6)	10.1
	C2 (C–O)	286.7 (1.6)	0.7	**O2 (C-O)**	533.7 (1.6)	1.2
	C3 (O=C–O)	289.3 (1.4)	0.5			**12.2**
	C4 (CO$_3$)	290.3 (1.2)	2.1			
			10.1	**Li1s**	56.1 (1.5)	45.6
				F1s	685.7 (1.5)	29.4
					687.6 (2.0)	1.4
				P2p$_{3/2}$	133.5 (1.7)	1.3

XPS binding energies (B.E. (eV)) of the different components of each core peak are reported with the full width at half maximum (FWHM (eV)) values between brackets. Atomic concentrations (%) corresponding to the different components are indicated. The total atomic percentage for each element is also given (in the last line). Note that it is not exactly the sum of the atomic percentages of all components in the specific case of the O 1s core peak as a weak contribution at low binding energies (resulting from minor charging effects) had to be added.

and can be also related to a few percent of species with a C=O bond.

After the reaction with 0.7 Li per CuO unit formula (point 1: 1.4 V/Li$^+$/Li), the C 1s spectrum does not show significant change. Three components can be always distinguished while the *C2* (C–O) and *C3* (O=C–O) peaks were respectively slightly shifted to 286.9 eV and 289.3 eV. Then, species containing C–O and O=C–O functional groups are present at the lithiated material surface in a very weak proportion (1.4% and 0.6% respectively). Furthermore, XPS analysis reveals that lithium and fluorine are the most abundant elements at point 1. The F 1s core peak (Fig. 3a) obtained for this sample is characterized by a main component at 685.6 eV, typical of LiF, and by a weak component at 687.7 eV assigned to Li$_x$PF$_y$ species (this binding energy is very close to the one measured for a LiPF$_6$ reference [25]). Then, the presence of a main LiF compound in the SEI layer at point 1 (30.5% of fluorine associated with LiF) can be confirmed by the Li 1s core peak position measured at 56.3 eV. Its formation at the electrode/electrolyte interface unambiguously results from the decomposition of the LiPF$_6$ salt. Furthermore, the XPS analysis has also revealed the presence of a very few amount of phosphorous in the sample ($\sim$2%). The P 2p$_{3/2-1/2}$ signal (Fig. 3b) recorded at point 1 consists of a main doublet at 134.2–135.2 eV assigned to phosphates [26] which also result from the decomposition of the LiPF$_6$ salt at the electrode/electrolyte interface. The doublet (very weak intensity) located at 137.1–138.1 eV is due to the presence of the Li$_x$PF$_y$ traces already mentioned. The formation of phosphates are confirmed by the presence of two main components in the O 1s signal, located at 531.2 (*O1*) and 532.1 eV (*O2*), which are characteristic of P=O and P– O$^-$ bonds respectively [27]. We can remind that oxygen atoms characteristic of the active material are not detected at point 1 due to the formation of a thick SEI layer at the electrode surface mainly made up of LiF. The selective formation of LiF at the beginning of the discharge (>1.4 V/Li$^+$/Li) could be explained by the preferentially decomposition/reduction of the LiPF$_6$ salt in this range of potential possibly influenced by the specific reactivity of the active material surface. Indeed, Younesi *et al.* [28] have recently shown that LiF is formed when a Li$_2$O$_2$ surface was simply exposed to a liquid electrolyte (LiPF$_6$ in PC or EC/DEC). Thus, their results suggest that LiPF$_6$ can be decomposed into LiF as soon as Li$_2$O$_2$ forms during the discharge. In our case, 'Li$_2$O$_2$' is formed during reduction of CuO and we also observe the presence of LiF.

After the second step of the discharge (point 2), as well as for other analysis points 3, 4 and 5, we observe the total disappearance of the LiF compound previously detected in large excess at the electrode surface (at point 1). This indicates that a fresh passivating layer (called "outer layer") with a thickness higher than the XPS analysis depth may be formed during the discharge below 1.4 V/Li$^+$/Li and covered the LiF-rich layer (called "inner layer") previously formed at higher discharge potentials. Furthermore, a modified C 1s core peak (Fig. 2a, point 3) is observed with the detection of a new component *C4* located at higher binding energies (*C4*: 290.3 eV). The components *C2* and *C3* present similar binding energies than those measured at point 1 with increased intensities. The C 1s core peak recorded at point 3 can be decomposed into four components located at 285.0, 286.7, 289.1 and 290.3 eV and assigned to –CH$_2$– CH$_2$–, C–O, O=C–O and CO$_3$ bonds, respectively (Fig. 2a, point 3).
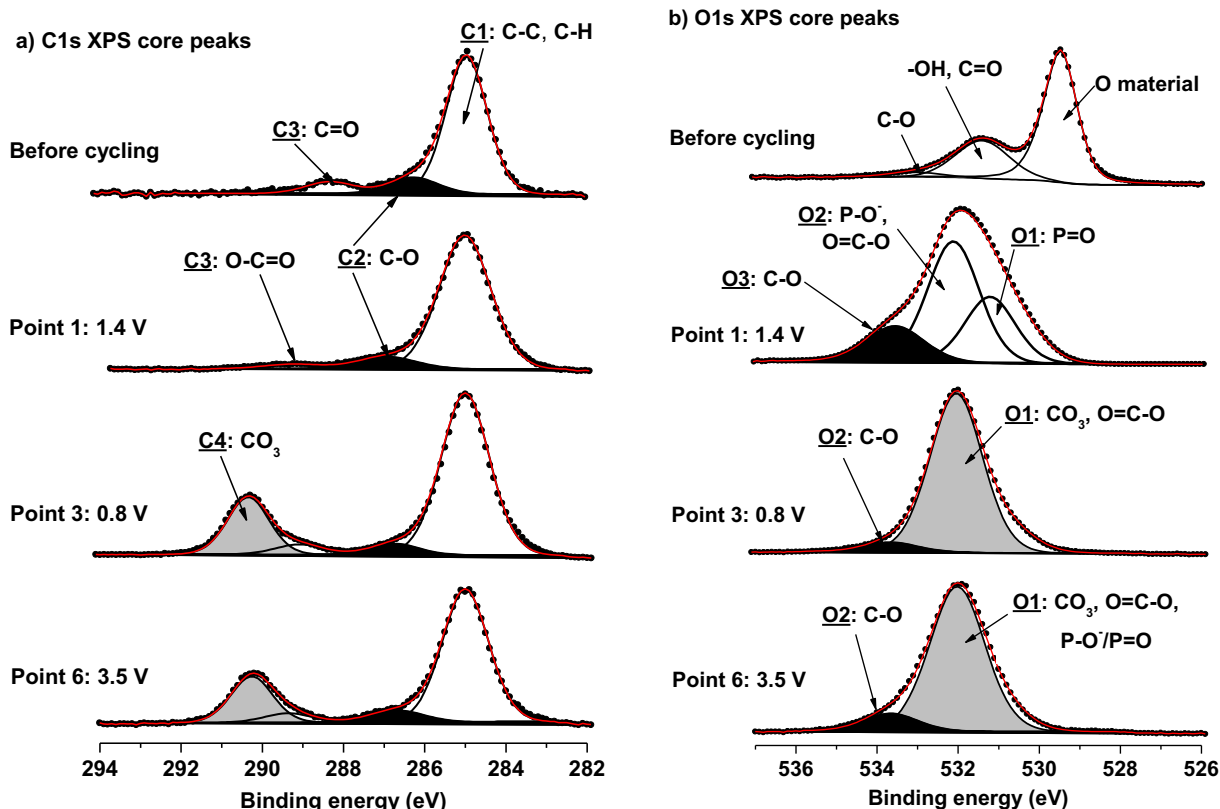
Fig. 2. XPS analyses of the C 1s (a) and O 1s (b) core peaks performed onto CuO thin film electrodes at different stages of the first voltammetric cycle: before cycling (CuO reference sample), after a discharge down to 1.4 V/Li$^+$/Li (point 1), at the end of the discharge (point 3) and at the end of the charge (point 6). Note that a small shoulder at low binding energies is present in the O 1s spectra of cycled samples, caused by the poor conductivity of SEI species. This shoulder results from minor charging effects.

Compared to point 1, the new peak *C4* (290.3 eV) characteristic of carbon bound to three oxygen atoms, is typical of carbonate-like species which could be Li_2CO_3 or alkyl carbonates $ROCO_2Li$ [29,30]. However, the presence of alkyl carbonate species should result in a peak of equal intensity at 290.3 eV (*C4*) and at 286.7 eV (*C2*) due to same number of carbon atoms present in a C—O and in a CO_3 environment. The quantitative analysis of the C 1s spectrum at the end of the discharge (point 3 in Table 1) gives a relative proportion for the *C4* and *C2* components equal to 4.4: 1.0. As this ratio is much higher than 1, we can thus mainly ascribe the *C4* component at 290.3 eV to inorganic lithium carbonate Li_2CO_3. In the O 1s core peak (Fig. 2b, point 3), oxygen atoms associated with Li_2CO_3 species represent the main contribution of the spectrum with the intense component *O1* located at 532.0 eV. The Li 1s peak collected for this sample is symmetrical and centered at 55.6 eV (FWHM = 1.6 eV), this binding energy being well characteristic of Li_2CO_3. The C 1s core peak analysis (Fig. 2a, point 3) also reveals the presence of a few percent of CO-like carbons (*C2* component: 1.9%) which can be explained by previously mentioned lithium alkyl carbonates and/or by other degradation products like ROLi or oligomers PEO $(-CH_2-CH_2-O-)_n$ [15], for which carbon atoms are in a one-oxygen environment. It can be noticed that the presence of species with C—O bonds is confirmed by the presence of a weak component *O2* at 533.7 eV in the O 1s spectrum. Finally, the analysis of the C 1s spectrum requires a last weak component *C3* at 289.1 eV which corresponds to COO-like carbons. This peak is often explained by the existence of lithium oxalate formed from CO_2 through some reductive processes. The possible formation of RCOOLi species was also proposed by Dedryvère et al. [18] to explain the detection of COO-like carbons at the surface of their lithiated CoO electrode. The atomic concentration measured for the

COO-like carbons is weak (1.7%) and the corresponding oxygen atoms exhibit the same binding energy as the main oxygen atoms present in the CO_3 environment. In conclusion, the XPS results have evidenced that the outer layer of the SEI is mainly constituted by inorganic Li_2CO_3 species from discharge potential of 1.0 V/Li$^+$/Li to subsequent charge potential of 2.6 V/Li$^+$/Li. This is consistent with previously reported results on the chemical composition of SEI formed on Cr_2O_3 thin film electrode [31].

At the end of the charge (point 6: 3.5 V/Li$^+$/Li), the C 1s spectrum has a similar shape to that obtained at point 3 and similar binding energies are measured for the four components. However, the atomic percentages of the different components (*C1* to *C4*) are lowered. The atomic concentration of carbons (*C4*) in a CO_3 environment is weak (2.1%) at the surface of the delithiated electrode. This highlights a modification of the passivating layer which can be explained by an efficient dissolution process of lithium carbonate species during the charge. The important evolution of the *C4* component intensity is directly in agreement with the modification of the corresponding *O1* component intensity (*O1* atomic percentage decreases from 27.0% (point 3) to 10.1% (point 6)). Furthermore, the XPS analysis performed at the end of the charge reveals the presence of LiF in a proportion similar to the one measured at point 1. The XPS signature of this compound is clearly identified with the presence of a main component at 685.7 eV in the F 1s core peak (Fig. 3c; 29.4% of fluorine associated with LiF) and with the binding energy position of the Li 1s core peak at 56.1 eV (LiF) instead of 55.6 eV (Li_2CO_3). Phosphates are also detected in a few percent at point 6 (Fig. 3d). It appears that the inner layer of the SEI (close to the electrode surface) formed at high potentials (>1.4 V/Li$^+$/Li) during the discharge, is observed again at the end of the charge as a consequence of the efficient dissolution process of
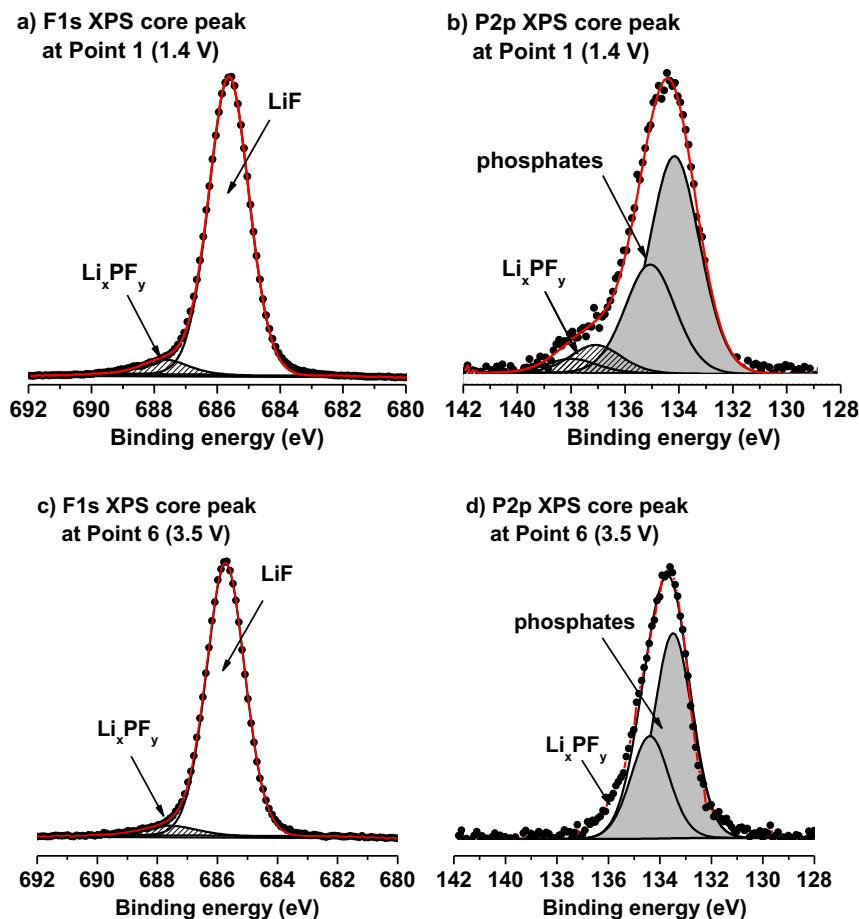
Fig. 3. XPS analysis of the F 1s and P 2p core peaks performed onto CuO thin film electrode at point 1 (a, b) and at point 6 (c, d).

the outer layer mainly made up of Li_2CO_3. We have thus demonstrated that a process of formation and partial dissolution of Li_2CO_3 species takes place during the first cycle of CuO thin film electrode. Moreover a remaining LiF-rich layer was detected at the end of the first charge which implies that some electrons and lithium ions are irreversibly consumed for its growth. This irreversible surface process thus contributes, with the partial irreversibility of the conversion reaction [7], to a capacity loss.
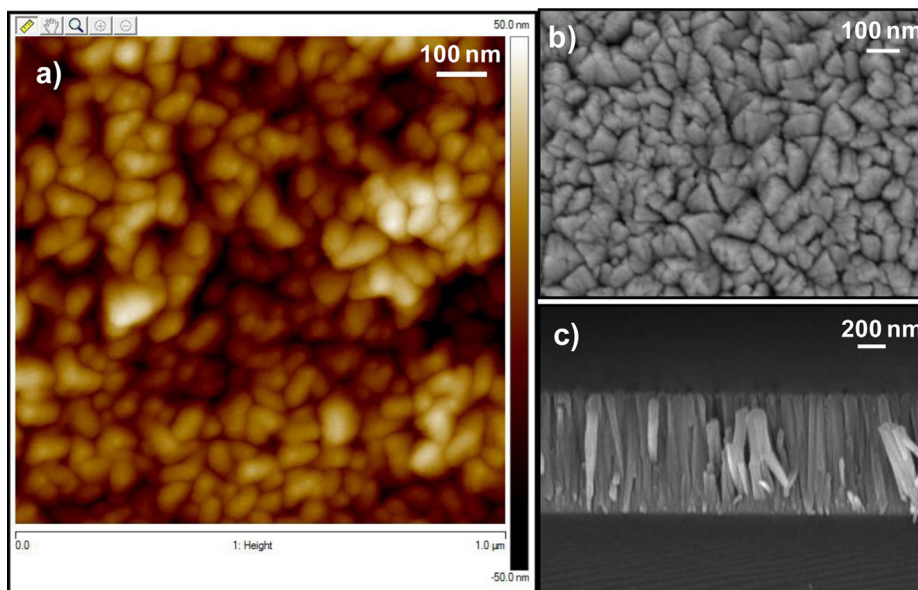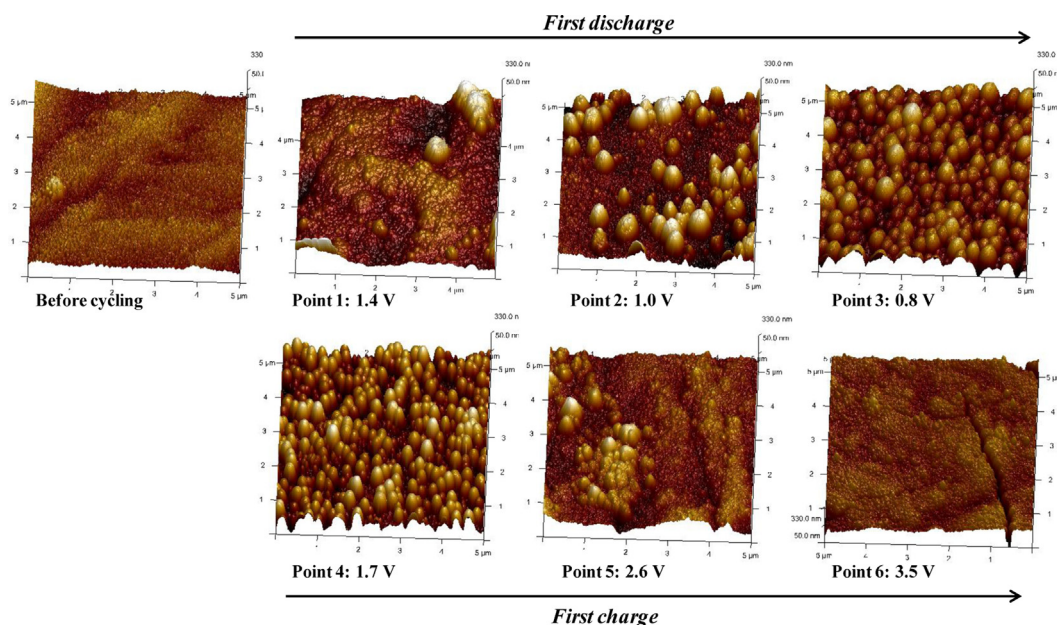

Fig. 4. Images of the pristine CuO thin film. AFM image of the surface (a) and SEM pictures of the surface (b) and cross-section (c).

Fig. 5. 3D AFM images (5 × 5 μm² scan size) of the CuO electrode surface at different stages of the first voltammetric cycle: before cycling (the pristine material) and different discharge/charge voltages (points 1–6).

3.1.2. AFM

The electrode surface was also investigated by means of AFM to observe morphological changes during cycling. Fig. 4a presents a 1 × 1 μm² AFM micrography of CuO sample deposited by reactive radio frequency magnetron sputtering without any intentional heating of the substrate. The CuO thin film surface consists in uniformly distributed grains having a pyramidal type shape and a grain size never exceeding 100 nm in the direction parallel to the substrate. The corresponding cross-section SEM image (Fig. 4c) reveals a porous thin film constituted by nano-columns with pyramidal heads (Fig. 4b).

Fig. 5 displays the topographical 5 × 5 μm² AFM images (presented in three dimensions with the same scale in z (nm) to allow an easy comparison) of the cycled CuO thin film electrodes at the

different discharge/charge potentials (Fig. 5: points 1–6) in comparison with the AFM image of the pristine material surface. The calculated R_q parameters are reported graphically on the Fig. 6 for the different analysis points.

3.1.2.1. Discharge. After a discharge down to 1.4 V/Li⁺/Li (point 1), the initial pyramid-shaped grains are no more detectable but a deposit seems to be present on the top of the film. This first result has to be correlated to the XPS analysis which demonstrates that a LiF-rich layer with a thickness at least higher than the XPS analysis depth is present at the electrode surface. So, at this stage, the observed deposit-like morphology can be related to the interfacial layer formed at the beginning of the first discharge. This morphological change is associated with an increase of the R_q roughness parameter from 27.3 to 58.3 nm (Fig. 6). Afterward, an important variation of the surface roughness is measured between the point 1 and the point 2 as the value of R_q continues to increase up to 93.7 nm. Indeed, when the CuO thin film electrode is discharged to 1.0 V/Li⁺/Li (point 2), large isolated particles are observed at the electrode surface and coexist with well-defined nanosized grains. The mean size of the nanograins (visible on Fig. 7b) is equal to 78.5 nm while the size of the large particles can easily reach 300–400 nm. The AFM image collected at point 2 (Fig. 7a) seems to indicate that the nanosized grains tend to be agglomerated which induces the formation of the larger particles at the electrode surface. Note that images recorded in "phase" mode at point 2 (not shown here) do not reveal any contrast which suggests that the mechanical properties of the different-sized grains are similar (homogeneous chemical nature for the surface). However, considering the grain size (for the small and the large ones), we cannot directly assign these grains (i.e. their entire volume) to the Li_2CO_3 phase identified by the XPS analysis. Note that the variation of the surface morphology and roughness may be caused by the formation of SEI and/or the conversion reaction as the insertion of Li⁺ ions induces volume expansion (the theoretical volume expansion is equal to 80% when CuO is fully converted into Cu/Li₂O). For the point 3, after a discharge down to 0.8 V/Li⁺/Li, the surface exhibits a uniform distribution of ~400 nm connected and spherical
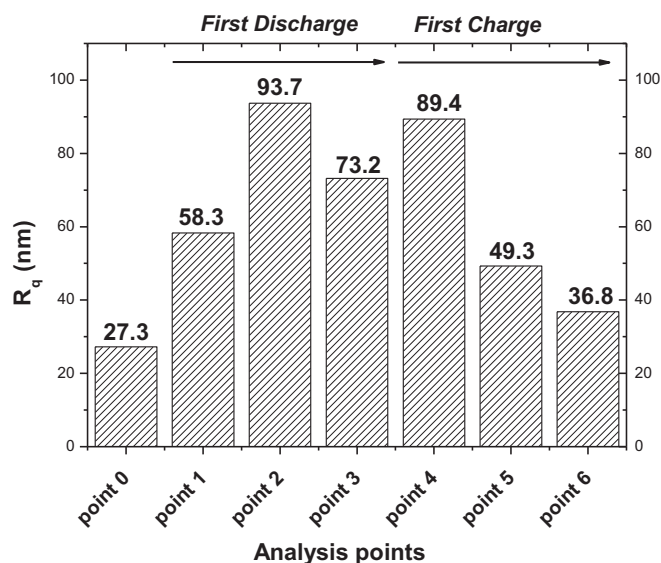
Fig. 6. R_q surface roughness measured from AFM images of the CuO thin film electrodes during the first voltammetric cycle.
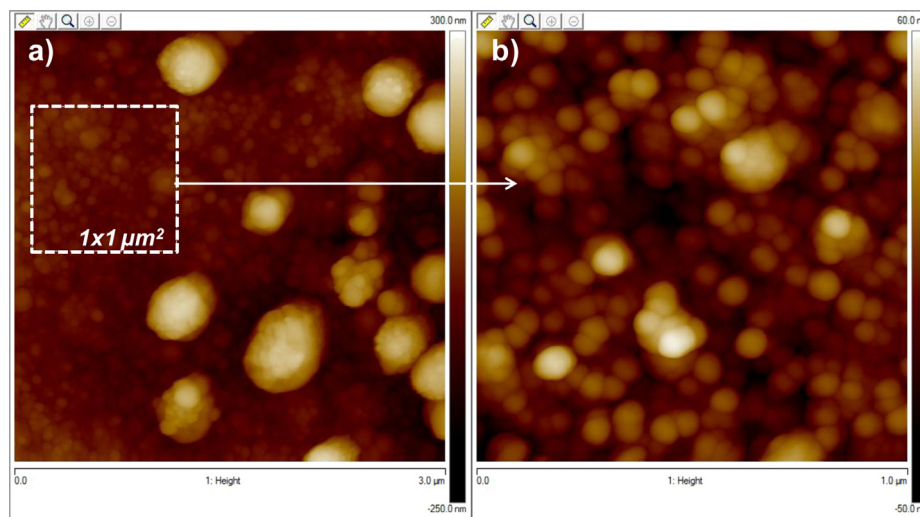
Fig. 7. 2D AFM images of the CuO electrode surface at point 2 (1.0 V/Li$^+$/Li): (a) 3 × 3 μm^2 image revealing large and nanosized grains and (b) 1 × 1 μm^2 image showing the well-defined nanograins.

particles. The formation of these large surface nodules has thus progressed between the discharge potentials of 1.0 and 0.8 V/Li$^+$/Li which generates a more compact and continuous layer at the electrode surface (Fig. 5, point 3). This evolution can thus explain the surface roughness decrease between points 2 and 3 (Fig. 6). These nodules can be characterized by their mean width (W_{nodule} = 406.0 nm) and their mean height (H_{nodule} = 177.5 nm). Note that these calculated mean values are deduced from numerous measurements of W_{nodule} and H_{nodule} performed on several topographic linear profiles.

*3.1.2.2. Charge.* After charging to 1.7 V/Li$^+$/Li (point 4), the large nodules are separated by area containing smaller grains which tends to be similar to the morphology of the point 2. The density of the large particles has thus decreased between the end of the discharge and the point 4 (beginning of the charge). Moreover their mean width has also decreased from 406.0 nm to 307.0 nm. The isolated large particles which remain at the electrode surface are thus responsible of the high surface roughness equal to 89.4 nm. An important evolution of the surface morphology is observed between the point 4 and the point 5 with the quasi-total disappearance of the large nodules at the electrode surface. Only few particles with a large size remain and the electrode surface becomes relatively smooth. Indeed, the roughness R_q has decreased from 89.4 nm (point 4) to 49.3 nm (point 5). Important morphological changes were thus evidenced between points 2 and 5 with the progressive formation (during discharge) and disappearance (during charge) of larger nodules. At the end of the charge (point 6), the electrode surface is quite smooth, no particles are visible and thus the roughness R_q is relatively close to the value measured for the pristine material (only ∼10 nm higher). In addition, well-defined cracks are evidenced by this AFM image (mean width = 123.0 nm and mean depth = 293.4 nm) showing that damages are caused by the volume variations of the electrode during the Li insertion/deinsertion cycles.

To summarize, a drastic increase of the grain size was observed during the discharge, from ∼70 nm to ∼400 nm, associated with a variation of the surface roughness from 27.3 nm to 73.2 nm. Then, the large particles of ∼400 nm totally disappeared during the charge and the surface roughness decreased to 36.8 nm. Note that very recent works also reported important surface morphology changes during the electrochemical cycling of different electrode

materials which were attributed to the SEI layer formation/partial dissolution process [32,12]. Zhang et al. [32] have investigated the SEI layer on MnO thin film electrodes (conversion material) using AFM imaging. The surface of their films exhibits grain size initially equal to ∼20 nm which drastically increased during the discharge reaching ∼200 nm (at 0.01 V/Li$^+$/Li) and then reversibly decreased during the charge to give a surface morphology similar to the initial one.

To explain the spherical morphology of the large particles (∼400 nm in width) generated in the discharge potential range of [1.4−0.8] V/Li$^+$/Li, we can propose that they probably result from amorphous structure (no structural anisotropy). Two hypotheses can be envisaged to explain their formation (Fig. 8): either the nodules consist in degradation products only and are thus associated with SEI deposit or they are made up of a "core" of lithiated active material and a SEI "shell". Note that the active material is constituted by nanoparticles of metallic copper (∼5 nm according to TEM images [33] (see Supporting information)) embedded in the lithiated active phases (mainly Li$_2$O) at the end of the discharge which induces a theoretical volume expansion of 80%. This is the maximum possible volume expansion associated with the conversion of CuO into Cu/Li$_2$O. We can thus propose that an extrusion process of some active phases could be caused by this volume expansion which generates the "core" of the nodule. Then, the active material extruded from the thin film is covered by a SEI layer which constitutes the "shell" (outer part) of the nodule. The last reduction step can be associated with a theoretical volume expansion of 13%, considering a mixing of the different active phases. This value is too low to possibly explain the formation of numerous large nodules at the electrode surface at the end of the first discharge, between points 2 and 3. Then, the size of larger nodules decreases during the first step of the charge (between points 3 and 4). The redox process which takes place in this potential range corresponds to the oxidation of a few amount of Li$_2$O into 'Li$_2$O$_2$' when 0.2 Li$^+$ ions were removed (very weak composition change of the active material). The corresponding volume contraction is thus negligible and cannot be responsible of the morphological change observed. Therefore, the formation and disappearance of the large nodules should be mainly related to the formation and decomposition of a huge amount of SEI species (Hyp. 1 in Fig. 8). These surface processes could be enhanced by the specific surface properties of the Li$_x$O$_y$/Cu composite material
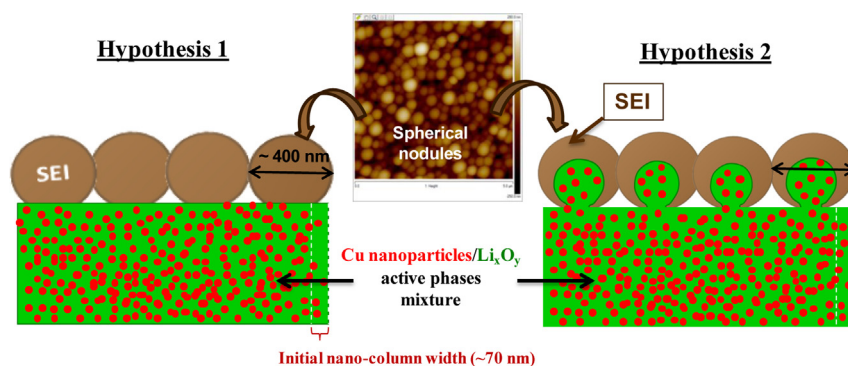
Fig. 8. Scheme illustrating the two different mechanisms proposed (hypotheses 1 and 2) to explain the possible origin of the large spherical nodules formed at the electrode surface during the first discharge.

detected from a discharge potential of 1.0 V/Li$^+$/Li to a charge potential of 2.6 V/Li$^+$/Li. We can thus propose that the agglomeration of nanograins made up of amorphous SEI phases could be at the origin of the progressive formation of large spherical nodules during the end of the discharge (between points 2 and 3). Then, the progressive decomposition of SEI phases induces size decrease and then the disappearance of the large particles at the electrode surface during the charge. This is consistent with the efficient dissolution process of Li$_2$CO$_3$ species evidenced by XPS analyses. Morales et al. [6] have also characterized the *liquid electrolyte/CuO (thin film)* interface but evidenced a thinner residual SEI layer than that observed in our conditions at the end of the first charge. Some differences can be noticed between these two studies like the surface morphology of the thin film (and thus of the specific surface), the composition of the liquid electrolyte and the cycling conditions used which lead to SEI layers with different properties. Hence, the thinner SEI layer observed at the electrode surface in the work of Morales *et al.* [6] may have favored the reversibility of the redox process which takes place within the thin film due to a possible smaller interfacial resistance. Indeed, the presence of Cu^{2+} ions has been evidenced by XPS analysis performed at the end of the charge in this previous work whereas only Cu$^+$ ions were detected in our thin film covered by a remaining thicker SEI layer.
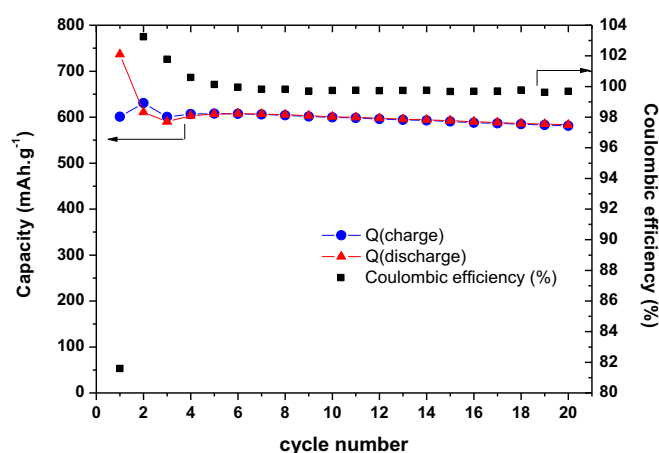
Fig. 9. Discharge capacity (in red), charge capacity (in blue) and coulombic efficiency (in black) are plotted as a function of cycle number. The two first cycles were carried out in a voltammetric mode (5 μV s^{-1}) while the 18 others were performed in a galvanostatic mode (weak current density of 6.6 μA cm^{-2}). (For interpretation of the references to color in this figure legend, the reader is referred to the web version of this article.)

3.2. Chemical and morphological evolution for subsequent cycles

Fig. 9 displays the evolution of the discharge and charge specific capacities as a function of the number of cycles, as well as the coulombic efficiency (see Supporting information for the voltage profiles recorded (Fig. s3)). After an initial loss of discharge capacity during the two first cycles, the capacity remains stable around 610 mAh g^{-1} for further cycles. At the second cycle, we can notice that the charge capacity is slightly higher than the discharge capacity which can result from one (or several) process(es) which is (are) more reversible at the second charge respect to the first charge (coulombic efficiency higher than 100). After 18 galvanostatic cycles (carried out after the two first voltammetric cycles), the capacity fading is quite low and equal to 1.8 mAh g^{-1} per cycle.

XPS and AFM analyses were carried out to probe the interfacial layer at different stages of the second voltammetric cycle and at the end of the 20th galvanostatic cycle. For a non-exhaustive presentation, some specific points which are associated with important results are discussed and compared to results of the first cycle (as the end of the 2nd discharge and charge and the end of the 20th charge).

3.2.1. XPS

As expected, the XPS analyses performed on samples discharge/charge during the second voltammetric cycle do not reveal the presence of copper at the electrode surface (Table 2). An interfacial layer with a thickness higher than the XPS analysis depth is thus still present during the second cycle.

At the end of the 2nd discharge, the chemical composition and relative percentage of SEI species (Table 2) are similar to those reported for the first discharge (point 3). At the level of the C1s spectrum (Fig. 10a), the four components (*C1* to *C4*) exhibit similar binding energies and the relative amount of *C4* (CO$_3$): *C2* (C–O) components, equal to 4.2: 1.0, is very close to that calculated at point 3. The atomic concentrations of CO$_3$-like carbons (*C4*: 10.0%) and oxygens (*O1*: 31.6%) evidence that these carbonates are present in a large proportion at the electrode surface. In conclusion, lithium carbonate Li$_2$CO$_3$ is the main compound of the outer SEI layer at the end of the 2nd discharge (as in the case of the 1st discharge) and it coexists with a few amount of other species having C–O (ethers, alkyl carbonates, …) and O=C–O (oxalate, carboxylate, …) functional groups. Note that only LiF traces (0.3% of fluorine) are detected at the end of the 2nd discharge, this compound being mainly present in the inner layer of the SEI.
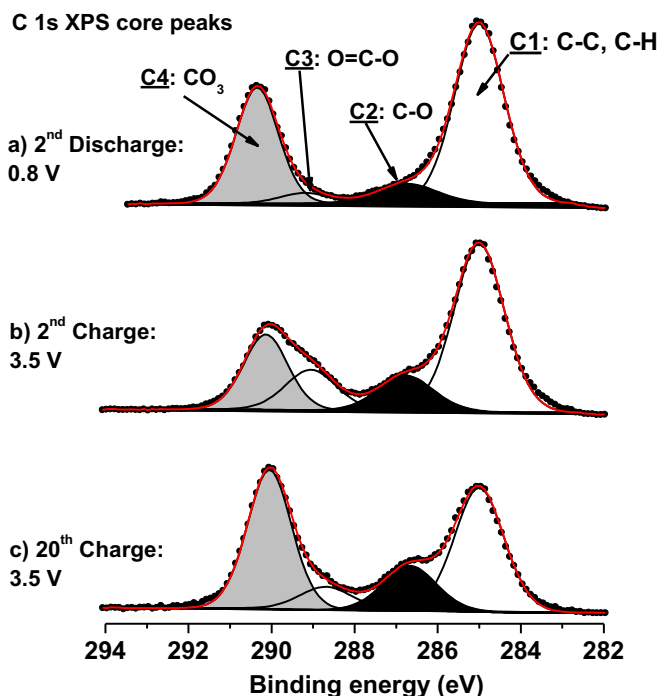
At the end of the 2nd charge (Fig. 10b), we can first notice that the intensity of the *C4* component assigned to carbonates species is much higher than that measured at point 6 (end of the first charge).

Table 2
Quantitative XPS analyses performed onto CuO thin film electrodes at two stages of the second voltammetric cycle (end of the discharge and charge) and at the end of the 20th galvanostatic cycle.

Potential (V/Li$^+$/Li)		B.E. (eV) (FWHM)	at. %		B.E. (eV) (FWHM)	at. %
2nd discharge, 0.8 V	**C1s**			**O1s**		
	C1 (C–C, C–H)	285.0 (1.4)	18.1	**O1 (CO$_3$)**	532.2 (1.5)	31.6
	C2 (C–O)	286.7 (1.5)	2.4	**O2 (C–O)**	533.9 (1.5)	1.4
	C3 (O=C–O)	289.2 (1.4)	1.1			**38.0**
	C4 (CO$_3$)	290.3 (1.2)	10.0			
			31.6	**Li1s**	55.7 (1.5)	30.1
				F1s	685.1 (1.5)	0.3
				P 2p$_{3/2}$	–	–
2nd charge, 3.5 V	**C1s**			**O1s**		
	C1 (C–C, C–H)	285.0 (1.4)	19.1	**O1 (CO$_3$)**	532.0 (1.5)	30.7
	C2 (C–O)	286.7 (1.6)	4.3	**O2 (C–O)**	533.6 (1.7)	3.0
	C3 (O=C–O)	289.0 (1.4)	4.6			**36.8**
	C4 (CO$_3$)	290.1 (1.2)	7.4			
			35.4	**Li1s**	55.5 (1.5)	25.4
				F1s	685.0 (1.5)	1.3
					687.1 (1.6)	0.3
				P2p$_{3/2}$	133.4 (1.6)	0.8
20th charge, 3.5 V	**C1s**			**O1s**		
	C1 (C–C, C–H)	285.0 (1.4)	10.8	**O1 (CO$_3$)**	531.9 (1.5)	36.8
	C2 (C–O)	286.7 (1.5)	4.1	**O2 (C–O)**	533.4 (1.6)	3.8
	C3 (O=C–O)	288.7 (1.5)	2.1			**40.6**
	C4 (CO$_3$)	290.0 (1.2)	10.7			
			27.7	**Li1s**	55.5 (1.5)	27.8
				F1s	685.1 (1.6)	1.9
					687.3 (2.0)	0.3
				P2p$_{3/2}$	133.4 (1.5)	0.9
				Cu2p$_{3/2}$	932.1 (1.3)	0.6
					933.1 (1.6)	0.2

XPS binding energies (B.E. (eV)) of the different components of each core peak are reported with the full width at half maximum (FWHM (eV)) values between brackets. Atomic concentrations (%) corresponding to the different components are indicated. The total atomic percentage for each element is also given (in the last line). Note that it is not exactly the sum of the atomic percentages of all components in the specific case of the O 1s core peak as a weak contribution at low binding energies (resulting from minor charging effects) had to be added.

Furthermore, the atomic concentration of CO$_3$-like carbons (C4) has only decreased from 10.0 to 7.4% between the end of the 2nd discharge and the end of the 2nd charge (Table 2). This decrease is low compared with the first cycle (ΔC%(CO$_3$) equal to −6.2% during the 1st charge and −2.6% during the 2nd charge). This first result thus reveals that the dissolution process of carbonates is less efficient during the second charge than during the first one. The higher proportion of remaining carbonates can explain that only a few percent of LiF species is detected at the end of the 2nd charge (1.3% of fluorine). Remind that the efficient dissolution of Li$_2$CO$_3$ allowed detecting again a large amount of LiF species (~30% of fluorine) at the end of the 1st charge. Moreover, the C2 and C3 components intensities have increased between the end of the 2nd discharge and the end of the 2nd charge (Table 2). The remaining SEI layer thus contains more species having C–O (like ROLi, PEO, alkyl carbonates species) and O=C–O (like oxalate and carboxylate species) functional groups. This modification of chemical composition can result from different dissolution efficiency of the different type of carbonaceous species (organic or inorganic species with C–O, O=C–O and CO$_3$ environments) present at the electrode surface. Indeed, Fleutot et al. [20] have observed by XPS that oxalates, PEO and ROLi species do not dissolve as well as lithium carbonates at the V$_2$O$_5$ thin film surface during the charge process between 1.5 and 3.7 V vs Li$^+$/Li. These XPS results have thus evidenced that the percentages of SEI species (with CO-, COO- and CO$_3$-like environments) are higher at the end of the 2nd charge respect to the end of the 1st charge (point 6) due to less efficient dissolution processes. The amount of remaining SEI species is thus more important at the end of the 2nd charge (extra Li amount devoted to the remaining SEI) which should lead to a loss of capacity at the second cycle (i.e. coulombic efficiency should be lower than 100%). However this loss of capacity is not evidenced by the electrochemical result (Fig. 9)

Fig. 10. XPS analyses of the C 1s core peak performed onto CuO thin film electrodes during the electrochemical cycling: (a) at the end of the 2nd discharge, (b) at the end of the 2nd charge and (c) at the end of the 20th charge.
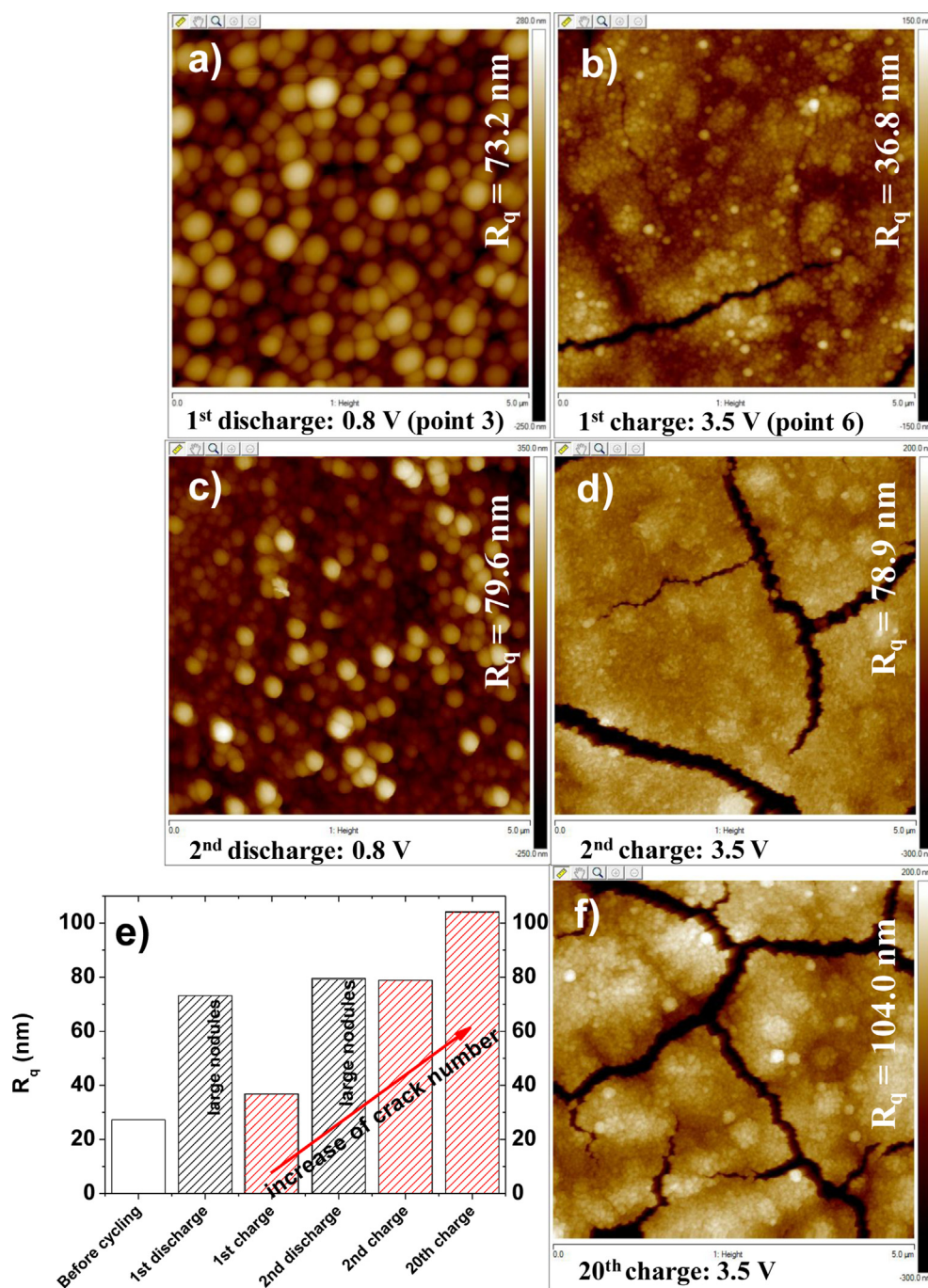
Fig. 11. AFM images (5 × 5 μm² scan size) of the CuO electrode surface at different stages of the first (a, b) and the second (c,d) voltammetric cycles and (f) at the end of the 20th charge. The R_q surface roughness measured from these AFM images are reported graphically (e).

due to a concomitant enhancement of the redox process reversibility which is responsible of the charge capacity increase for the second cycle (i.e. coulombic efficiency higher than 100%).

At the end of the 20th charge, the chemical composition of the SEI has slightly evolved respect to the 2nd charge (Table 2, Fig. 10c). The main difference concerns the carbonates which are present in a higher proportion than that measured at the end of the 2nd charge (10.7% of CO_3-like carbons instead of 7.4%). This result indicates that their partial dissolution is less and less efficient during the cycling. Moreover, we can also notice that copper ($\sim$1%) is detected again at the electrode surface after 20 cycles. The possible explanations will be discussed after the related AFM results.

3.2.2. AFM

The evolution of the surface morphology of cycled CuO thin films has been studied by AFM at the second and the twentieth cycles (Fig. 11). As already mentioned, some cracks were observed on films at the end of the first charge (Fig. 11b). Then, these cracks disappear during the subsequent discharge (Fig. 11c) as the thin film expands again during the Li insertion, filling the voids. The AFM image acquired at the end of the 2nd discharge (Fig. 11c) reveals a surface morphology similar to the one observed at the end of the first discharge (Fig. 11a) with the presence of large nodules having a round shape. However, their size is slightly smaller and characterized by a mean width value equal to 315.9 nm (2nd
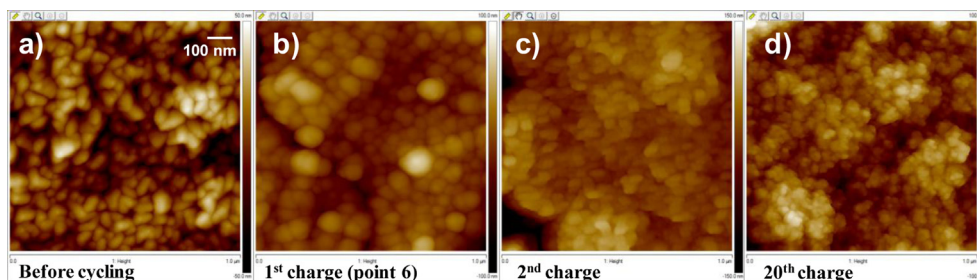
Fig. 12. AFM images (1×1 μm^2 scan size) of the CuO electrode surface at different stages of the cycling: before cycling (a) and at the end of the first (b), second (c) and 20th (d) charges.

discharge) instead of 406.0 nm (1st discharge). This difference does not significantly affect the R_q parameter as close values are measured at the end of the first and the second discharge (Fig. 11e). The formation of the large particles at the electrode surface thus systematically occurs during the discharge. The most probable hypothesis (Hyp. 1) envisaged to explain their formation is related to the agglomeration of grains made up of SEI phases. This SEI growth could be affected by the electrode surface properties which continuously evolve during cycling and this can explain the slight different morphologies observed at the first and at the second discharges.

At the end of the 2nd charge (Fig. 11d), we observe the disappearance of the large nodules previously formed during the discharge which proves that the formation/disappearance process of these nodules is reproducible. Furthermore, the fracture of the thin film electrode (Fig. 11d) has progressed by comparison with the first charge (Fig. 11b). Indeed, the amount of cracks has increased as well as their mean width (from 123.0 to 294.6 nm) and their mean depth (from 293.4 to 415.2 nm) and being consistent with the important increase of the R_q parameter between the end of the first and the second charges (increase from 36.8 to 78.9 nm).

The damages of the thin film appear even more important at the end of the 20th charge (Fig. 11f) as a network of cracks divides the thin film surface into isolated islets and leads to an increase of the R_q parameter value up to 104 nm. We can conclude that the progressive appearance of cracks in the cycled CuO thin film is induced by repetitive volume expansion/contraction undergone by the conversion material during the lithium insertion/deinsertion cycles. The detection of a very weak percentage of copper at the end of the 20th charge by XPS is explained by the fracture of the thin film which reveals fresh surfaces and possibly internal electronically isolated parts of the electrode film.

Complementary magnified images (1×1 μm^2 scan size) of "plane" surface region (without cracks) are also presented on Fig. 12 to well characterize the surface morphology of the thin film electrode at the end of the different charges. For the first charge (point 6), a relatively thin deposit appears to take the exact shape of the CuO grains (before cycling). Then, the deposit thickness observed at the end of the second charge and at the end of the twentieth charge seems to progressively increase with the presence of a larger amount of SEI phases. This morphological evolution can thus support the XPS results which have indicated that the percentage of remaining carbonates species increases with the number of cycles. However, the important evolution of surface properties (chemical and morphological changes) observed by XPS and AFM analyses during cycling does not significantly affect the electrochemical performances of the thin film electrode as the gravimetric capacity remains stable and the coulombic efficiency is close to 100% for the 20 cycles. The conversion mechanism is thus effective during the first 20 cycles despite the progressive thin film cracking and the less reversible formation/dissolution SEI process.

4. Conclusion

This study explored the formation of the SEI layer on CuO thin film electrode cycled in a lithium cell containing a EC, DMC, PC, LiPF$_6$ based electrolyte and its evolution during cycling. Correlations were established between composition and morphological changes of the electrode surface and can be summarized as follows:

- During the first discharge, the growth of a stratified surface layers between the lithiated CuO electrode and the liquid electrolyte was evidenced and mainly consists of LiF in the inner part (close to the electrode) and Li$_2$CO$_3$ in the outer part (close to the electrolyte). Simultaneously to the Li$_2$CO$_3$-rich layer formation (below 1.4 V/Li$^+$/Li during the discharge), large nodules with a round shape are progressively forming and covering the electrode surface. At the end of the first charge, an efficient dissolution of the carbonates species was revealed by XPS analysis and the large nodules disappear according to the AFM image. Then, considering two possible mechanisms, it was proposed that the formation/disappearance of the large nodules originates in the formation/dissolution of a huge amount of SEI species. Finally, a residual LiF-rich deposit was identified which partially explain the loss of capacity noticed at the end of the first voltammetric cycle and the partial reversibility of the redox process.
- During subsequent cycles, the reversible formation/disappearance of the large nodules is still observed. Moreover, XPS quantitative analyses show an increase of the residual deposit as the percentage of the remaining carbonates species increases with the number of charges. This result was confirmed by AFM analyses: a thicker and thicker residual deposit is identified at the electrode surface. Then, concomitant to the degradation of the carbonates dissolution process during cycling, a progressive cracking of the cycled CuO thin film was observed with the formation of pronounced cracks during the charge (volume contraction) and their filling-in during the discharge (volume expansion). These evolutions, associated with the progressive accumulation of SEI species observed at the end of the various charges, do not induce a noticeable change of the reversible capacity over cycles. After 20 cycles, a specific capacity and a coulombic efficiency respectively close to 600 mAh g^{-1} and 100% are reached.

Appendix A. Supplementary data

References

[1] P. Poizot, S. Laruelle, S. Grugeon, L. Dupont, J.-M. Tarascon, Nature 407 (2000) 496–499.
[2] J. Cabana, L. Monconduit, D. Larcher, M. Palacin, Adv. Mater. 22 (2010) E170–E192.

[3] R. Bates, Y. Jumel, Lithium Batteries, Academic Press, London, 1983.
[4] S. Grugeon, S. Laruelle, R. Herrera-Urbina, L. Dupont, P. Poizot, J.-M. Tarascon, J. Electrochem. Soc. 148 (2001) A285–A292.
[5] A. Debart, L. Dupont, P. Poizot, J.-B. Leriche, J.-M. Tarascon, J. Electrochem. Soc. 148 (2001) A1266–A1274.
[6] J. Morales, L. Sanchez, F. Martin, J. Ramos-Barrado, M. Sanchez, Electrochim. Acta 49 (2004) 4589–4597.
[7] L. Martin, H. Martinez, D. Poinot, B. Pecquenard, F. Le Cras, J. Phys. Chem. C 117 (2013) 4421–4430.
[8] E. Peled, D. Golodnitsky, G. Ardel, J. Electrochem. Soc. 144 (1997) L208–L210.
[9] D. Aurbach, M. Levi, E. Levi, A. Schechter, J. Phys. Chem. B 101 (1997) 2195–2206.
[10] D. Aurbach, J. Power Sources 89 (2000) 206–218.
[11] K. Edstrom, M. Herstedt, D. Abraham, J. Power Sources 153 (2006) 380–384.
[12] S. Bhattacharya, A. Alpas, Carbon 50 (2012) 5359–5371.
[13] S. Chattopadhyay, A. Lipson, H. Karmel, J. Emery, T. Fister, P. Fenter, M. Hersam, M. Bedzyk, Chem. Mater. 24 (2012) 3038–3043.
[14] J. Lee, N. Nitta, J. Benson, A. Magasinski, T. Fuller, G. Yushin, Carbon 52 (2013) 388–397.
[15] G. Gachot, S. Grugeon, M. Armand, S. Pilard, P. Guenot, J.-M. Tarascon, S. Laruelle, J. Power Sources 178 (2008) 409–421.
[16] L. Dupont, S. Laruelle, S. Grugeon, C. Dickinson, W. Zhou, J.-M. Tarascon, J. Power Sources 175 (2008) 502–509.
[17] Y. Zeng, L. Li, H. Li, X. Huang, L. Chen, Ionics 15 (2009) 91–96.
[18] R. Dedryvere, S. Laruelle, S. Grugeon, P. Poizot, D. Gonbeau, J.-M. Tarascon, Chem. Mater. 16 (2004) 1056–1061.
[19] S. Laruelle, S. Grugeon, P. Poizot, M. Dollé, L. Dupont, J.-M. Tarascon, J. Electrochem. Soc. 149 (2002) A627–A634.
[20] B. Fleutot, H. Martinez, B. Pecquenard, J. Ledeuil, A. Levasseur, D. Gonbeau, J. Power Sources 180 (2008) 836–844.
[21] L. Martin, H. Martinez, M. Ulldemolins, B. Pecquenard, F. Le Cras, Solid State Ionics 215 (2012) 36–44.
[22] D. Shirley, Phys. Rev. B: Condens. Matter Mater. Phys. 5 (1972) 4709–4714.
[23] J. Scofield, J. Electron Spectrosc. Relat. Phenom. 8 (1976) 129–137.
[24] F. Parmigiani, G. Pacchioni, F. Illas, P. Bagus, J. Electron Spectrosc. Relat. Phenom. 59 (1992) 255–269.
[25] P. Verma, P. Maire, P. Novak, Electrochim. Acta 55 (2010) 6332–6341.
[26] R. Dedryvere, S. Laruelle, S. Grugeon, L. Gireaud, J.-M. Tarascon, D. Gonbeau, J. Electrochem. Soc. 152 (2005) A689–A696.
[27] B. Fleutot, B. Pecquenard, H. Martinez, M. Letellier, A. Levasseur, Solid State Ionics 186 (2011) 29–36.
[28] R. Younesi, M. Hahlin, F. Björefors, P. Johansson, K. Edström, Chem. Mater. 25 (2013) 77–84.
[29] K. Xu, Chem. Rev. 104 (2004) 4303–4417.
[30] R. Dedryvere, L. Gireaud, S. Grugeon, S. Laruelle, J.-M. Tarascon, D. Gonbeau, J. Phys. Chem. B 109 (2005) 15868–15875.
[31] J.-T. Li, V. Maurice, J. Swiatowska-Mrowiecka, A. Seyeux, S. Zanna, L. Klein, S.-G. Sun, P. Marcus, Electrochim. Acta 54 (2009) 3700–3707.
[32] J. Zhang, R. Wang, X. Yang, W. Lu, X. Wu, X. Wang, H. Li, L. Chen, Nano Lett. 12 (2012) 2153–2157.
[33] D. Poinot, PhD thesis, Bordeaux University, 2011.